View Article Online
View Journal

Nanoscale Horizons

The home for rapid reports of exceptional significance in nanoscience and nanotechnology

Accepted Manuscript

This article can be cited before page numbers have been issued, to do this please use: L. Biondelli, E. A. Podshivaylov, Y. Ding, W. Stradley, U. Filippi, P. A. Frantsuzov and M. K. Kuno, *Nanoscale Horiz.*, 2026, DOI: 10.1039/D5NH00801H.

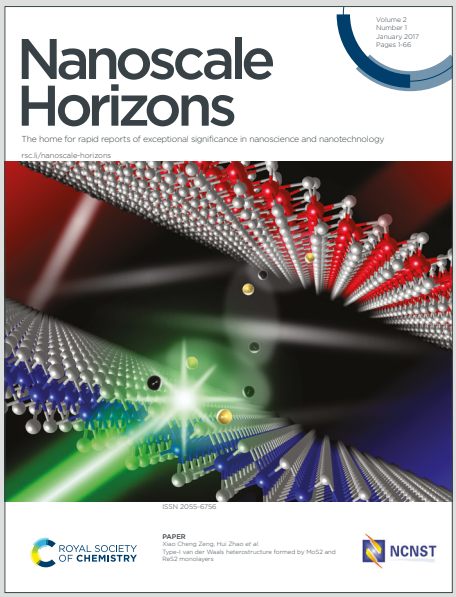

New Concepts

View Article Online
DOI: 10.1039/D5NH00801H

In this work, we establish that mid-infrared (MIR) photothermal contrast contains significant contributions from light scattered by the specimen and its local dielectric environment. While existing literature attributes MIR photothermal contrast primarily to competing photothermal-induced changes in specimen refractive indices and volumes, our study identifies that contrast contains significant contributions from an interference between light scattered from a specimen's surrounding medium and back-reflected probe light. We model and experimentally confirm this mechanism, demonstrating a predicted, small-particle size crossover in contrast when particles are embedded in air versus Nujol. This breakthrough provides fundamental insight into the origins of MIR photothermal contrast in images and spectra. It further offers new opportunities for conducting single-particle MIR super-resolution absorption measurements in complex environmental matrices.

View Article Online
DOI: 10.1039/D5NH00801H

Journal Name

ARTICLE TYPE

Cite this: DOI: 00.0000/xxxxxxxxxx

Local environment influence on mid-infrared photothermal contrast

Linda Biondelli,[a,‡] Eduard Podshivaylov[b,‡] Yang Ding,[a] Walker Stradley,[a] Umberto Filippi,[c,d] Pavel Frantsuzov,[b] and Masaru Kuno,[*,a,d]

Received Date
Accepted Date

DOI: 00.0000/xxxxxxxxxx

Abstract. Mid-infrared (MIR) photothermal microscopy and spectroscopy represents a new, ultrasensitive, superresolution infrared absorption technique. The origin of its signal contrast is complex, containing competing contributions from photothermal-induced changes to specimen refractive indices and volumes as well as those of the local environment. In this study, we investigate the interplay between abovementioned thermo-optic/thermal expansion contributions to observed contrast in MIR photothermal microscopy images and spectra. This entails size-dependent measurements on individual polystyrene and polymethylmethacrylate nanoparticles with radii below 100 nm and as low as 25 nm. From this, we now establish that sizable photothermal contrast arises from the interference between light scattered from a specimen's local dielectric medium and backreflected light from an air/substrate interface. This is particularly important for small specimens embedded in media. Attesting to this, we observe, for the first time, a predicted, small nanoparticle size crossover in signal contrast between particles embedded in air versus a dielectric medium with a refractive index greater than one.

1 Introduction

Infrared (IR) absorption microscopy/spectroscopy is widely used in materials science[1], chemistry[2], and biology[3] because it is a sensitive, non-destructive, label-free, and chemically specific analysis. Unfortunately, its spatial resolution is limited by the Abbe diffraction limit. For IR wavelengths between 2.5–10 μm, resulting spatial resolutions are of order $\sim$5 μm. This prevents traditional IR microscopy from being used to conduct high spatial resolution chemical analyses.

To address this limitation, various superresolution IR techniques have been developed to conduct measurements below the IR diffraction limit.[4, 5] This includes atomic force microscope (AFM)-based photothermal infrared (AFM-PTIR or AFM-IR) microscopy.[6–8] It also includes scanning near-field versions that employ tips to locally enhance and scatter IR light.[9–11] Tip-based techniques, however, suffer from issues related to the need for specimens to possess sizable thermal expansion coefficients as well as the occasional complexity of measured signals.

Scanning transmission electron microscope electron energy loss spectroscopy (STEM-EELS) is another superresolution IR technique.[12–15] It can achieve a 1-2 nm spatial resolution, depending on sample thickness, beam conditions, and detector sensitivity. STEM-EELS, however, has limitations due to specimen beam damage, the need for specialized EELS spectrometers to approach energies close to the Rayleigh line, and the need to operate in vacuum.

An all-optical, tabletop, superresolution technique that has recently gained traction, is optical photothermal infrared spectroscopy (O-PTIR)[1, 16–24], alternatively called infrared photothermal heterodyne imaging (IR-PHI). The technique achieves a spatial resolution of $\sim$300 nm and has been used in various capacities to image individual cells[18], virus particles[18], polymer beads[18, 21, 25], micro/nanoplastics[26, 27], metal nanostructures[28, 29], and semiconductors.[30–32]

An open question for O-PTIR/IR-PHI is the origin of its contrast in obtained mid-infrared (MIR) images and spectra.[25] The technique operates via local photothermal heating of materials following their on-resonance excitation. What results are induced changes to material refractive indices (n) as well as transient changes to associated volumes. If a surrounding medium is present, for example, in biological imaging applications where water is present, it also leads to subsequent localized heating and corresponding changes to the medium's refractive index, n_{m}.

[a] University of Notre Dame, Department of Chemistry and Biochemistry, Notre Dame, IN 46556 USA
[c] Department of Nanochemistry, Istituto Italiano di Tecnologia, 16163 Genova, Italy
[b] Voevodsky Institute of Chemical Kinetics and Combustion SB RAS, 630090 Novosibirsk, Russia
[d] University of Notre Dame, Department of Physics and Astronomy, Notre Dame, IN 46556 USA
‡ Contributed equally
† Supplementary Information available. See DOI: 00.0000/00000000.

View Article Online
DOI: 10.1039/D5NH00801H

As illustration of the ambiguity surrounding O-PTIR/IR-PHI signal contrast, analogous single particle (visible wavelength) photothermal measurements employ a surrounding medium's refractive index as the primary reporter for specimen absorption.[33] This stems from small specimen sizes, which lead to efficient heat transfer into the surrounding medium. O-PTIR/IR-PHI measurements, by contrast, are generally medium free. Samples are simply dispersed onto substrates and are nominally surrounded by air ($n_m \simeq 1$) absent an unintentional hydration layer.

Even without surrounding medium contrast contributions, O-PTIR/IR-PHI signal contrast possesses a complex origin due to contributions from both specimen refractive index and transient volumetric changes. This is unlike AFM-PTIR/AFM-IR where contrast arises solely from the thermal expansion of probed specimens. Modeled O-PTIR/IR-PHI probe backscattering cross sections take the general form[18, 25]

$$\Delta\sigma_{\text{backscat}} = \left(\frac{\partial\sigma_{\text{backscat}}}{\partial n}\frac{\partial n}{\partial T} + \frac{\partial\sigma_{\text{backscat}}}{\partial r}\frac{\partial r}{\partial T}\right)\Delta T \equiv \Delta\sigma_n + \Delta\sigma_r \quad (1)$$

where ΔT is the induced temperature change in the specimen and where $\frac{\partial n}{\partial T}$ and $\frac{\partial r}{\partial T}$ are specimen thermo-optic and thermal expansion coefficients, respectively with $\Delta\sigma_n = \left(\frac{\partial\sigma_{\text{backscat}}}{\partial n}\frac{\partial n}{\partial T}\right)\Delta T$ and $\Delta\sigma_r = \left(\frac{\partial\sigma_{\text{backscat}}}{\partial r}\frac{\partial r}{\partial T}\right)\Delta T$. Notably, $\frac{\partial n}{\partial T}$ and $\frac{\partial r}{\partial T}$ adopt opposite signs. $\Delta\sigma_n$ and $\Delta\sigma_r$ contributions to $\Delta\sigma_{\text{backscat}}$ therefore counteract each other and possibly contain complex specimen size and refractive index dependencies. Ambiguity therefore exists over the primary contribution to O-PTIR/IR-PHI signal contrast and to the role a local environment plays, if present.

2 Experimental

Here, we employ a widefield version of O-PTIR/IR-PHI, called wIR-PHI, to study the origin of its photothermal contrast. The widefield modality employs a tunable MIR (pump) laser (MSquared, Firefly LW, 20 kHz, 1840-1042 cm^{-1}) in conjunction with a pulsed, visible (probe) laser (Thorlabs, NPL52C, 515 nm, ~129 ns, 40 kHz) and a high speed, complementary metal oxide semiconductor (CMOS) camera (Photron, FASTcam Nova S12, 40 kHz) to image specimens. A counterpropagating pump/probe geometry maximizes the technique's spatial resolution given that the visible probe establishes its effective diffraction limit. Pump, probe, and camera frame acquisition are synchronized using a programmable pulse generator (Quantum Composers, Emerald). **Figure 1** is a general scheme of the instrument. **Figure 1b** shows example images of individual $r = 134$ and $r = 94$ nm PMMA NPs where visible ripples result from differences in probe laser diffraction due to NP size variations when "hot" versus "cold". This has been discussed in Reference [21]. More details about the instrument along with a timing diagram of pump, probe, and camera synchronization pulses can be found in the manuscript's Supplementary Information (SI).

Specimens consist of different-sized polymethylmethacrylate (PMMA) and polystyrene (PS) nanoparticles (NPs) to establish wIR-PHI contrast size-dependencies. To assess environmental contributions to observed MIR contrast, nanoparticles are embedded in an IR compatible oil, Nujol. PMMA NP radii (r) range from ~140-30 nm [$r = 134 \pm 11$ nm; 94 ± 8 nm; 56 ± 4 nm; 28 ± 5 nm]. PS NP radii range from ~100-25 nm [$r = 106 \pm 7$ nm; 51 ± 5 nm; 39 ± 6 nm; 24 ± 4 nm]. In what follows, different-sized particles are referred to using their mean radii. The SI provides sample sizing images and histograms as well as more information on specimen preparation wherein nanoparticles are dropcast onto CaF_2 coverslips (Crystran, 200 μm). For specimens surrounded by Nujol, a Nujol solution of particles is first made before spincoating suspensions onto CaF_2 coverslips.

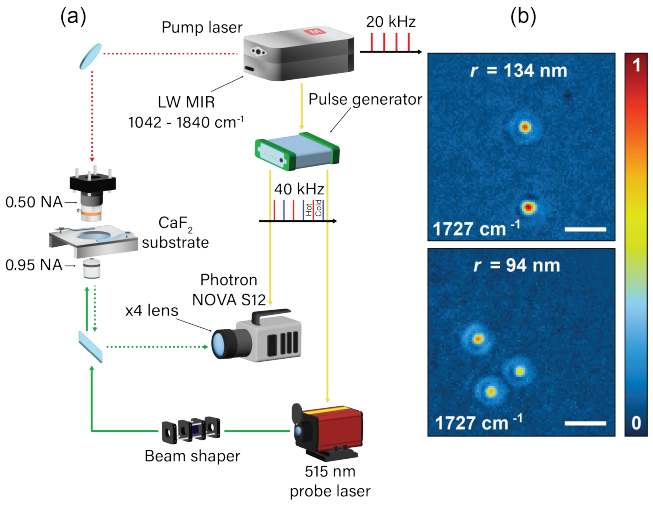

Fig. 1 (a) Schematic of the wIR-PHI instrument. (b) Representative 1727 cm^{-1} C=O stretch images of individual $r = 134$ and $r = 94$ nm PMMA nanoparticles. Scale bars: 500 nm.

wIR-PHI images are obtained by irradiating the NPs with the MIR pump at 20 kHz ($I_{\text{pump,1727 cm}^{-1}\text{,PMMA}}$=448.4 kW cm^{-2}, $I_{\text{pump,1450 cm}^{-1}\text{,PS}}$=500.8 kW cm^{-2}, both for all sizes). Induced photothermal changes for a ~ 3 K (~ 30 K) temperature change to PS (PMMA) NPs are probed with the visible laser, operating at 40 kHz ($I_{\text{probe}} = 219$ kW cm^{-2}). For additional details about temperature changes induced in the NPs by the pump laser, refer to the SI.

Probe pulses are coincident and interspaced between pump pulses. CMOS images, acquired at 40 kHz, record "hot" (pump and probe pulses coincident) and "cold" (probe pulse interspaced between pump pulses) images from where their difference gives rise to MIR contrast. Hyperspectral images and spectra are acquired by scanning the MIR laser frequency (1042-1840 cm^{-1}) during data acquisition. Reference [21] provides a general description of the wIR-PHI technique. Subsequent instrument upgrades, including addition of beam shaping optics to produce uniform intensity distributions as well as simplifications to the optics to increase pump and probe power throughputs, have improved the instrument's sensitivity/limit-of-detection. The SI provides more details about these modifications.

3 Results and Discussion

Figure 1b shows representative 1727 cm^{-1} (PMMA C=O stretch) wIR-PHI images of individual $r = 134$ nm and $r = 94$ nm PMMA NPs. **Figures 2a-d** show additional 1727 cm^{-1} wIR-PHI images

View Article Online
DOI: 10.1039/D5NH00801H

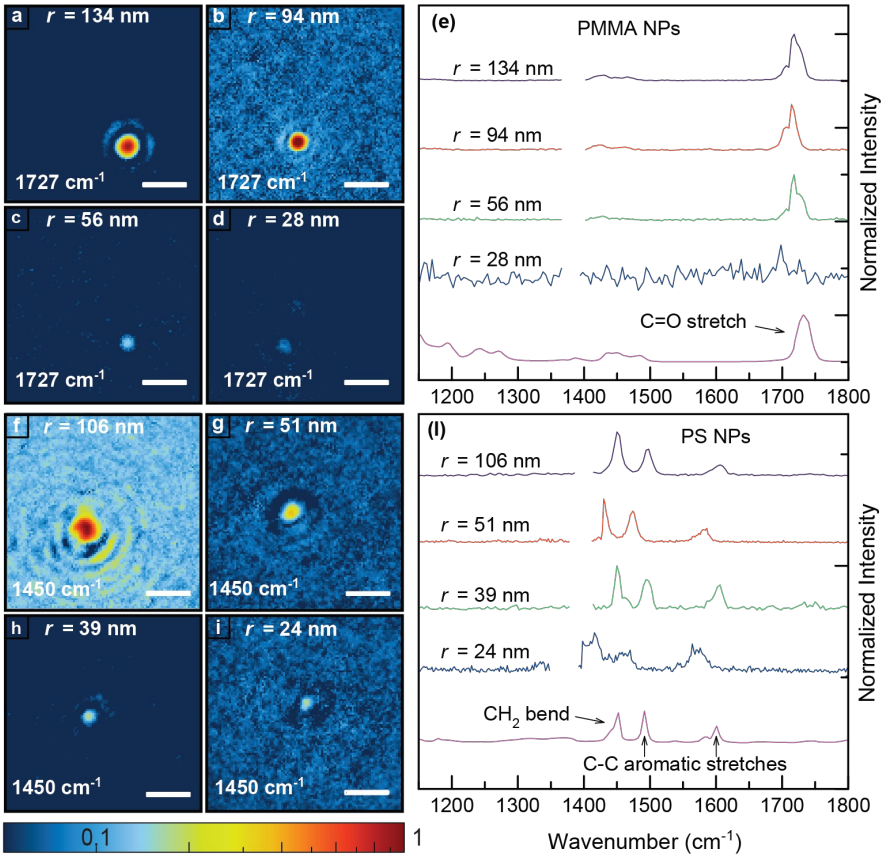

Fig. 2 Normalized 1727 cm^{-1} wIR-PHI images of individual (a) $r = 134$ nm, (b) $r = 94$ nm, (c) $r = 56$ nm, and (d) $r = 28$ nm PMMA nanoparticles. Normalized 1450 cm^{-1} wIR-PHI images of individual (f) $r = 106$ nm, (g) $r = 51$ nm, (h) $r = 39$ nm, and (i) $r = 24$ nm PS nanoparticles. Images plotted on logarithmic scales. Scale bars: 500 nm. (e,l) Corresponding single particle wIR-PHI spectra: Spectra normalized to 1 and offset for clarity. For either PMMA or PS, literature reference spectra in purple.[34, 35]

across the full PMMA size range. **Figures 2f-i** show analogous 1450 cm^{-1} (PS CH_2 bend) PS NP images across the studied size range. In total, ~80 NPs from both PMMA and PS size series have been studied [PMMA w/o Nujol: $r = 134$ nm ($N = 8$); $r = 94$ nm ($N = 9$); $r = 56$ nm ($N = 7$); $r = 28$ nm ($N = 4$); PMMA w. Nujol: $r = 134$ nm ($N = 5$); $r = 94$ nm ($N = 7$); $r = 56$ nm ($N = 8$); $r = 28$ nm ($N = 7$); PS: $r = 106$ nm ($N = 6$); $r = 51$ nm ($N = 9$); $r = 39$ nm ($N = 11$); $r = 24$ nm ($N = 4$)].

Figures 2e,l provide corresponding, individual PMMA and PS NP spectra, acquired using wIR-PHI's hyperspectral modality. In either case, comparison of acquired spectra to reference PMMA and PS spectra (bottom, purple) reveal good agreement with expected PMMA C=O and PS CH_2 bend/C-C aromatic stretches. Observed spectral shifts, relative to reference spectra, likely stem from variations of the local absorber environment. In whole, acquired spectra agree with prior IR-PHI and wIR-PHI data of individual PMMA and PS nanoparticles.[21, 25] The SI provides additional, single particle hyperspectral images and spectra.

Figures 3a and **3c** summarize observed, size-dependent, average wIR-PHI signals from individual PMMA and PS nanoparticle measurements. wIR-PHI signal values fall monotonically with size and agree with prior PMMA and PS IR-PHI data.[21, 25]

Figures 3b and **3d** summarize associated signal-to-noise ratios (SNRs). For PMMA, SNR-values are as large as ~ 156 in larger NPs. For PS, SNR-values as high as ~ 73 are seen. For $r < 50$ nm, whether PMMA or PS, improvements to the wIR-PHI instrument now yield larger average SNR-values than previously reported. Most illustrative of this is that $r = 28$ ($r = 24$) nm PMMA (PS) particles are now observable with a SNR value of 8.2 (11.6). This contrasts with previous efforts where only $r > 50$ nm PMMA or PS NPs could be detected using either IR-PHI[25] or wIR-PHI.[21]

In descending order by size, acquired PMMA NP SNR-values are 139.2 ± 25.6 ($r = 134$ nm), 100.3 ± 12.7 ($r = 94$ nm), 12.6 ± 2.0 ($r = 56$ nm), and 6.8 ± 1.0 ($r = 28$ nm). Corresponding PS NP SNR-values are 73.4 ± 20.2 ($r = 106$ nm), 31.5 ± 19.9 ($r = 51$ nm), 26.5 ± 11.5 ($r = 39$ nm), and 11.6 ± 2.3 ($r = 24$ nm). Using a defined, limit-of-detection (LOD) of SNR = 5 and a linear fit to the SNR data (dashed blue line, **Figure 3b**), we obtain a new, 1727 cm^{-1} PMMA NP LOD of $r_{LOD} = 22$ nm. For PS (**Figure 3d**, dashed blue line), an estimated 1450 cm^{-1} LOD is $r_{LOD} = 15$ nm. In terms of absorption cross section (σ), the new PMMA LOD is $\sigma_{LOD,1727\ cm^{-1}} \sim 3.33 \times 10^{-13}$ cm^2. For PS, it is $\sigma_{LOD,1450\ cm^{-1}} \sim 1.5 \times 10^{-14}$ cm^2. This latter value compares favorably to $\sigma_{LOD,1450\ cm^{-1}} = 3 \times 10^{-14}$ cm^2 reported previously.[25] The SI provides details of these σ_{LOD} estimates.

To rationalize above observed behavior, specimen refractive

View Article Online
DOI: 10.1039/D5NH00801H

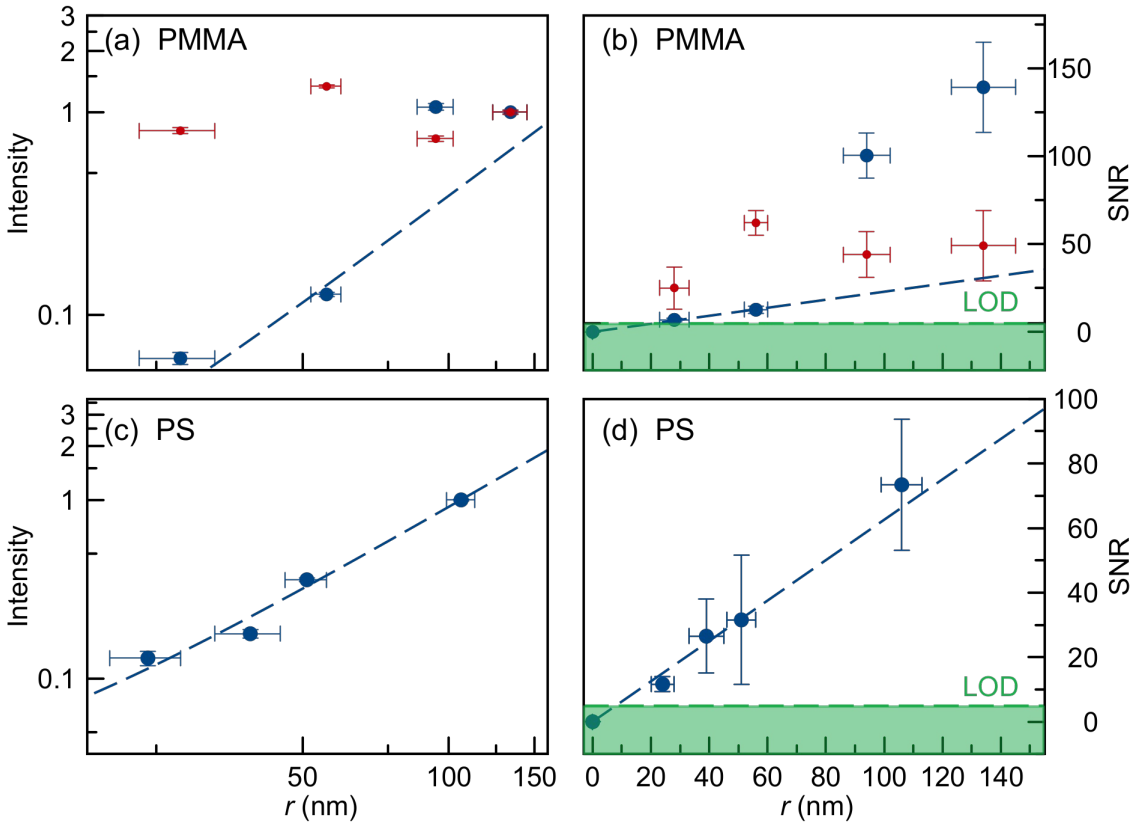

Fig. 3 (a,c) Normalized average wIR-PHI signals for different-sized (a) PMMA and (c) PS nanoparticles. Normalization relative to the largest nanoparticle size in each case. (b,d) Corresponding SNR-values for (b) PMMA and (d) PS NPs. Blue (red) symbols represent data acquired in air (Nujol). Dashed blue lines, linear SNR fits to the smallest NP sizes. Green horizontal dashed lines, SNR-defined LOD.

index and transient volumetric changes to $\Delta\sigma_{backscat}$ in **Equation 1** have been modeled. **Figure S38** plots contributions of both $\Delta\sigma_n$ and $\Delta\sigma_r$ to $\Delta\sigma_{backscat}$ as functions of particle size for PMMA NPs in air. Theoretical estimates employ PMMA's thermo-optic $\left(\frac{\partial n}{\partial T} = -1.2\times10^{-4}\,^{\circ}\mathrm{C}^{-1}\right)$[36] and thermal expansion $\left(\frac{1}{r}\frac{\partial r}{\partial T} = 7\times10^{-5}\,^{\circ}\mathrm{C}^{-1}\right)$[37] coefficients. $n_m = 1$ has been assumed to model the surrounding medium as done previously.[25]

From a comparison to experiment, it emerges that for PMMA NPs with sizes between $r = 50-150$ nm, the dominant contribution to $\sigma_{backscat}$ (i.e., their wIR-PHI signal contrast) is the specimen's thermo-optic coefficient. This follows the conclusion previously reported in Reference [25]. We also observe that for sufficiently small particles (r <50 nm), $\Delta\sigma_n$ and $\Delta\sigma_r$ contributions are near equal, leading to a significantly diminishment of $\Delta\sigma_{backscat}$.

We now investigate the role of the surrounding medium's refractive index on wIR-PHI contrast by conducting experiments with PMMA NPs embedded in Nujol. Nujol oil has been used because it possesses MIR vibrational resonances that do not strongly overlap with those of PMMA. The infrared spectrum of Nujol oil is reported in the SI. Unfortunately, the same is not true with PS given overlap of Nujol's 1450 cm^{-1} resonance with PS's 1450 cm^{-1} CH_2 bend. Other solvents such as Fluorolube with large MIR transparency windows were considered. None were found to be as compatible with PMMA (or PS) as Nujol.

Figures 4 a-d show results of wIR-PHI measurements across the studied PMMA size range in the absence of Nujol. Individual PMMA NP 1727 cm^{-1} SNR-values are 156 ($r = 134$ nm), 109 ($r = 94$ nm), 14 ($r = 56$ nm), and 8 ($r = 28$ nm). **Figures 4e** and **4f** show corresponding 1727 cm^{-1} images of individual $r = 134$ nm and $r = 94$ nm NPs in Nujol. Images were acquired under the same experimental conditions as for specimens without Nujol. Observed SNR-values are 58 ($r = 134$ nm) and 50 ($r = 94$ nm). **Table 1** summarizes average PMMA NP SNR-values without and with a Nujol environment.

Table 1 PMMA nanoparticle average SNR-values without and with a Nujol environment.

r (nm)	SNR w/o Nujol	SNR w. Nujol
134	139.2 ± 25.6	49 ± 20
94	100.3 ± 12.7	44 ± 13
56	12.6 ± 2.0	62 ± 7
28	6.8 ± 1.0	25 ± 12

Of particular note is a SNR reversal for $r = 56$ and $r = 28$ nm PMMA nanoparticles in **Figures 4g** and **4h**. Specifically, their Nujol environment SNR-values are ~ 63 ($r = 56$) and ~ 28 ($r = 28$ nm). This contrasts to ~ 14 ($r = 56$) and ~ 8 ($r = 28$ nm) without Nujol. Evident is an approximate five-fold SNR enhancement. For larger NPs, the opposite is true and Nujol environment SNR-values are approximately five-fold smaller than corresponding

View Article Online
DOI: 10.1039/D5NH00801H

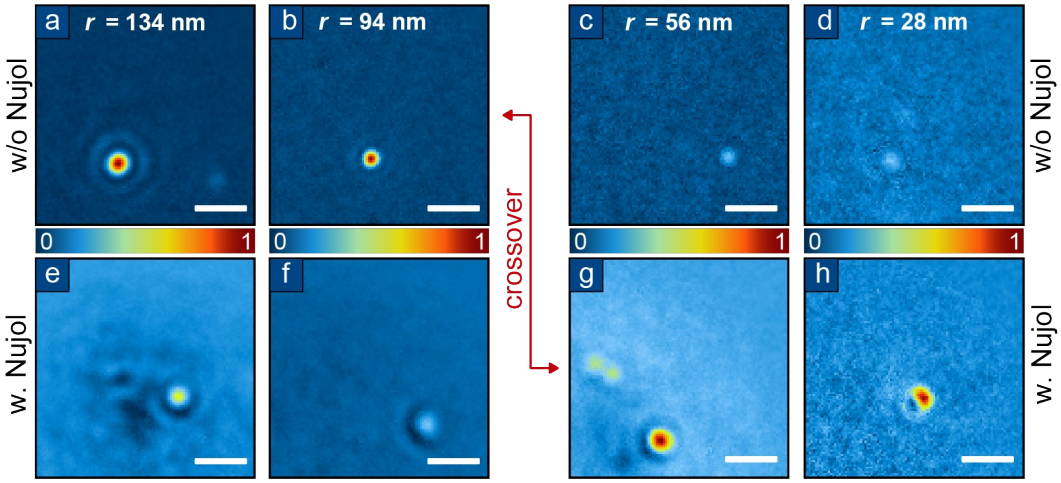

Fig. 4 1727 cm^{-1} wIR-PHI images of individual PMMA NPs without (a, b, c, d) and with (e, f, g, h) a Nujol surrounding medium. Pictures are paired by size and are normalized relative to one another. Scale bars: 500 nm.

SNR-values without Nujol. We therefore observe an environment-induced crossover in wIR-PHI signal contrast for PMMA NP sizes of order $r \sim 75$ nm.

Although the above wIR-PHI signal modeling predicts a significant diminishment of $\Delta\sigma_{backscat}$ at small NP sizes, the above data point to the existence of complex environmental dependencies. Some hints of this exist in the data. Backscattering cross sections for small particles should exhibit a r^6 size dependency due to Rayleigh scattering. **Figure 3**, however, reveals more gradual changes of wIR-PHI contrast with r^α where $\alpha = 1-2$ ($\alpha_{PMMA} = 1.79$ and $\alpha_{PS} = 1.58$).

Because **Equation 1** does not consider any scattering contributions from the broader dielectric environment (i.e., substrate and medium) surrounding a specimen, it has been modified. Interactions of all fields scattered into the far field by the probed specimen while in the presence/absence of the MIR pump laser (denoted "hot" and "cold" in what follows) are now considered. In the absence of a MIR pump, the total electric field scattered by a "cold" system contains two contributions,

$$\boldsymbol{E}^{cold}_{total} = \boldsymbol{E}^{cold}_{NP} + \boldsymbol{E}_{refl}, \tag{2}$$

where $\boldsymbol{E}^{cold}_{NP}$ is the backscattered probe field from a cold NP and $\boldsymbol{E}_{refl}$ is the reflected probe field at the air/substrate interface atop which the particle sits.[38] This is similar to scattering considerations that are part of Interferometric Scattering (iSCAT) microscopy.[39] **Figure 5a** illustrates a schematic of the NP specimen sitting atop a CaF_2 substrate along with the relevant air/CaF_2 interface.

The total electric field scattered by a "hot" specimen similarly consists of three contributions,

$$\boldsymbol{E}^{hot}_{total} = \boldsymbol{E}^{hot}_{NP} + \boldsymbol{E}_{m} + \boldsymbol{E}_{refl}, \tag{3}$$

with $\boldsymbol{E}^{hot}_{NP}$ the backscattered probe field from a hot NP and $\boldsymbol{E}_m$ the backscattered field from the hot (surrounding) medium (**Figure 5b**).[40, 41] Heat transfer from the irradiated NP to the medium is therefore considered. The observed wIR-PHI signal is then proportional to the difference in power between hot and cold specimens,

$$S \propto \left|\boldsymbol{E}^{hot}_{total}\right|^2 - \left|\boldsymbol{E}^{cold}_{total}\right|^2. \tag{4}$$

Detailed evaluations of $\boldsymbol{E}^{cold}_{NP}$, $\boldsymbol{E}^{hot}_{NP}$, and $\boldsymbol{E}_{refl}$ have been provided in the SI.

The above modeling indicates that for specimens embedded in a dielectric medium, the observed wIR-PHI signal contrast arises from two interferences. The first is between the scattered field from the NP and the reflected probe field at the air/substrate interface. The second is between the scattered field from the NP's surrounding medium and the same reflected probe field at the air/substrate interface. This latter interaction was not considered earlier in Reference [25].

When a NP's surrounding dielectric medium is air, as in Reference [25], an evaluation of **Equation 4** shows that wIR-PHI's signal contrast is primarily due to the following difference

$$S_{air} \propto \mathrm{Re}\left(\left[\boldsymbol{E}^{hot}_{NP} - \boldsymbol{E}^{cold}_{NP}\right]\cdot\boldsymbol{E}^{*}_{refl}\right). \tag{5}$$

This is because the electric field associated with light scattered by air has a negligible magnitude compared to either $\boldsymbol{E}^{hot}_{NP}$ or $\boldsymbol{E}^{cold}_{NP}$ (**Figure S36**). In **Equation 5**, the electric field difference in brackets is related to our earlier discussion about competing contributions of $\Delta\sigma_n$ and $\Delta\sigma_r$ to $\Delta\sigma_{backscat}$. As seen in **Figure S38**, this difference means that $S_{air} \to 0$ for small NPs.

In Nujol, $\Delta\sigma_{backscat}$ does not experience a $\Delta\sigma_n/\Delta\sigma_r$ cancellation at small NP sizes. This is highlighted in **Figure S40**, which shows $\Delta\sigma_n$ dominating $\Delta\sigma_r$ for all r. The wIR-PHI signal power in this case is given by

$$S_{nujol} \propto \mathrm{Re}\left(\boldsymbol{E}_m\cdot\boldsymbol{E}^{*}_{refl}\right) + \mathrm{Re}\left(\left[\boldsymbol{E}^{hot}_{NP} - \boldsymbol{E}^{cold}_{NP}\right]\cdot\boldsymbol{E}^{*}_{refl}\right). \tag{6}$$

An explicit evaluation of **Equation 6** is carried out in the SI. The analysis shows that wIR-PHI's signal contrast in Nujol is enhanced relative to that seen in air for NP sizes below $r \sim 110$ nm. Above $r \sim 110$ nm, the signal contrast in air is larger than in Nujol. The model thus successfully predicts a crossover of wIR-PHI

View Article Online
DOI: 10.1039/D5NH00801H

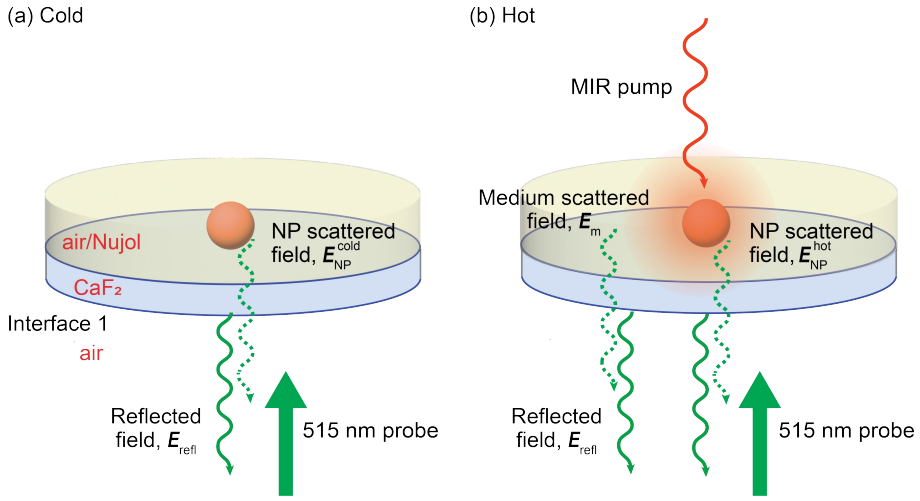

Fig. 5 Specimen schematic, consisting of polymer NPs deposited atop CaF_2 substrates. Air/Nujol dielectric environment surrounding the NP depicted in light yellow. Air/CaF_2 interface depicted. (a) Cold conditions without MIR irradiation. (b) Hot conditions with MIR irradiation.

signal contrast in Nujol over air at small sizes (see **Figure S41**), in excellent agreement with the $r \sim 75$ nm crossover reported in **Figure 4**.

At a microscopic level, the developed model reveals that at small NP sizes ($r \lesssim 50$ nm, **Figure S39**), the main contribution to wIR-PHI signal contrast is the interference between the field scattered by the heated local medium, which surrounds a specimen, and the reflected probe field at the air/substrate interface. This agrees with the conclusions of Berciaud et al.[40, 41] who find that visible photothermal microscopy's detection limit is primarily dictated by the thermal response of a specimen's surrounding dielectric medium.

Conclusions

The current study refines our understanding about the origin of MIR contrast in O-PTIR/IR-PHI photothermal images and spectra. Through combined widefield and hyperspectral measurements on individual PMMA and PS nanoparticles with radii as low as $r \sim 25$ nm, we now establish that O-PTIR/IR-PHI MIR contrast contains contributions from light scattered by the specimen and by its local dielectric environment. In particular, accompanying theoretical modeling indicates that the observed wIR-PHI contrast is complex and involves interference contributions between the reflected probe field and that of the NP as well as its surrounding dielectric medium. The latter dominates for media where $n_m > 1$. A notable success of the model is its prediction of a small particle size crossover in photothermal contrast for particles embedded in air versus Nujol, which occurs due to the interference between light scattered from a specimen's surrounding (hot) medium and backreflected probe light. This aligns with existing, visible wavelength, photothermal studies and paves the way for future, single particle MIR superresolution absorption measurements as well as studies in complex environmental matrices.

Author contributions

L. Biondelli: experiment, data analysis, and manuscript preparation, E. Podshivaylov: theoretical modeling, Y. Ding: experiment, Walker Stradley: experiment, U. Filippi: data analysis, P. Frantsuzov: theoretical modeling, M. Kuno: experiment design, data analysis and manuscript preparation.

ORCID IDs

- Linda Biondelli: 0009-0000-6058-8780
- Eduard A. Podshivaylov: 0000-0001-9521-8296
- Yang Ding: 0000-0001-8437-3565
- Walker Stradley: 0009-0001-2069-229X
- Umberto Filippi: 0009-0004-2126-8206
- Pavel Frantsuzov: 0000-0002-7717-5453
- Masaru Kuno: 0000-0003-4210-8514

Conflicts of interest

There are no conflicts to declare.

Data availability

Data supporting this article have been included as part of the Supplementary Information.

Acknowledgements

We thank Skerxho Osmani for assistance with the experiment. We also thank Kristian Ziu and Alexey Koslov for assistance with writing the Python data acquisition program. This work was supported by the National Science Foundation (CHE-1954724). Instrument development was supported by the Division of Materials Sciences and Engineering, Office of Basic Energy Sciences, U.S. Department of Energy (Award DE-SC0014334). Partial support from the University of Notre Dame, Notre Dame Global and the Luksic Foundation is acknowledged. Theoretical efforts by E.P. and P.F. were supported by core funding from the Russian Federal Ministry of Science and Higher Education (FWGF-2021-0002).

Notes and references

1 C. B. Prater, M. Kansiz and J.-X. Cheng, *APL Photonics*, 2024, **9**, 091101.

View Article Online
DOI: 10.1039/D5NH00801H

2 J. Haas and B. Mizaikoff, *Annual Review of Analytical Chemistry*, 2016, **9**, 45–68.
3 Á. I. López-Lorente and B. Mizaikoff, *Analytical and Bioanalytical Chemistry*, 2016, **408**, 2875–2889.
4 I. M. Pavlovetc, K. Aleshire, G. V. Hartland and M. Kuno, *Physical Chemistry Chemical Physics*, 2020, **22**, 4313–4325.
5 A. Centrone, *Annual Review of Analytical Chemistry*, 2015, **8**, 101–126.
6 A. Lahrech, R. Bachelot, P. Gleyzes and A. Boccara, *Optics Letters*, 1996, **21**, 1315–1317.
7 A. Dazzi, R. Prazeres, F. Glotin and J. Ortega, *Optics Letters*, 2005, **30**, 2388–2390.
8 J. J. Schwartz, D. S. Jakob and A. Centrone, *Chemical Society Reviews*, 2022, **51**, 5248–5267.
9 B. Knoll and F. Keilmann, *Nature*, 1999, **399**, 134–137.
10 R. Hillenbrand and F. Keilmann, *Physical Review Letters*, 2000, **85**, 3029.
11 H. A. Bechtel, E. A. Muller, R. L. Olmon, M. C. Martin and M. B. Raschke, *Proceedings of the National Academy of Sciences*, 2014, **111**, 7191–7196.
12 V. Kumar and J. P. Camden, *The Journal of Physical Chemistry C*, 2022, **126**, 16919–16927.
13 F. J. García de Abajo, *Reviews of Modern Physics*, 2010, **82**, 209–275.
14 J. A. Hachtel, A. R. Lupini and J. C. Idrobo, *Scientific Reports*, 2018, **8**, 5637.
15 M. Varela, A. R. Lupini, K. v. Benthem, A. Y. Borisevich, M. F. Chisholm, N. Shibata, E. Abe and S. J. Pennycook, *Annu. Rev. Mater. Res.*, 2005, **35**, 539–569.
16 R. Furstenberg, C. A. Kendziora, M. R. Papantonakis, V. Nguyen and R. McGill, Next-Generation Spectroscopic Technologies V, 2012, pp. 293–302.
17 A. Mërtiri, T. Jeys, V. Liberman, M. Hong, J. Mertz, H. Altug and S. Erramilli, *Applied Physics Letters*, 2012, **101**, 44101.
18 Z. Li, K. Aleshire, M. Kuno and G. V. Hartland, *The Journal of Physical Chemistry B*, 2017, **121**, 8838–8846.
19 P. D. Samolis and M. Y. Sander, *Optics Express*, 2019, **27**, 2643–2655.
20 E. M. Paiva and F. M. Schmidt, *Analytical Chemistry*, 2022, **94**, 14242–14250.
21 K. Kniazev, E. Zaitsev, S. Zhang, Y. Ding, L. Ngo, Z. Zhang, G. V. Hartland and M. Kuno, *ACS Photonics*, 2023, **10**, 2854–2860.
22 M. Tamamitsu, K. Toda, M. Fukushima, V. R. Badarla, H. Shimada, S. Ota, K. Konishi and T. Ideguchi, *Nature Photonics*, 2024, **18**, 738–743.
23 D. Zhang, C. Li, C. Zhang, M. N. Slipchenko, G. Eakins and J.-X. Cheng, *Science Advances*, 2016, **2**, e1600521.
24 Y. Bai, D. Zhang, L. Lan, Y. Huang, K. Maize, A. Shakouri and J.-X. Cheng, *Science Advances*, 2019, **5**, eaav7127.
25 I. M. Pavlovetc, E. A. Podshivaylov, R. Chatterjee, G. V. Hartland, P. A. Frantsuzov and M. Kuno, *Journal of Applied Physics*, 2020, **127**, 165101.
26 K. Kniazev, I. M. Pavlovetc, S. Zhang, J. Kim, R. L. Stevenson, K. Doudrick and M. Kuno, *Environmental Science & Technology*, 2021, **55**, 15891–15899.
27 O. Nwachukwu, K. Kniazev, A. Abarca Perez, M. Kuno and K. Doudrick, *Environmental Science & Technology*, 2024, **58**, 1312–1320.
28 K. Aleshire, I. M. Pavlovetc, R. Collette, X.-T. Kong, P. D. Rack, S. Zhang, D. J. Masiello, J. P. Camden, G. V. Hartland and M. Kuno, *Proceedings of the National Academy of Sciences*, 2020, **117**, 2288–2293.
29 N. Baden, H. Watanabe, M. Aoyagi, H. Ujii and Y. Fujita, *Nanoscale Horizons*, 2024, **9**, 1311–1317.
30 Y. Yuan, J. Chae, Y. Shao, Q. Wang, Z. Xiao, A. Centrone and J. Huang, *Advanced Energy Materials*, 2015, **5**, 1500615.
31 R. Chatterjee, I. M. Pavlovetc, K. Aleshire, G. V. Hartland and M. Kuno, *ACS Energy Letters*, 2018, **3**, 469–475.
32 I. M. Pavlovetc, M. C. Brennan, S. Draguta, A. Ruth, T. Moot, J. A. Christians, K. Aleshire, S. P. Harvey, S. Toso, S. U. Nanayakkara *et al.*, *ACS Energy Letters*, 2020, **5**, 2802–2810.
33 A. Gaiduk, P. V. Ruijgrok, M. Yorulmaz and M. Orrit, *Chemical Science*, 2010, **1**, 343–350.
34 F. Huth, A. Govyadinov, S. Amarie, W. Nuansing, F. Keilmann and R. Hillenbrand, *Nano letters*, 2012, **12**, 3973–3978.
35 D. Olmos, E. Martín and J. González-Benito, *Physical Chemistry Chemical Physics*, 2014, **16**, 24339–24349.
36 R. M. Waxler, D. Horowitz and A. Feldman, *Applied Optics*, 1979, **18**, 101–104.
37 R. Haward and A. Trainor, *Journal of Materials Science*, 1974, **9**, 1243–1251.
38 H. Zong, C. Yurdakul, Y. Bai, M. Zhang, M. S. Unlu and J.-X. Cheng, *ACS photonics*, 2021, **8**, 3323–3336.
39 N. S. Ginsberg, C.-L. Hsieh, P. Kukura, M. Piliarik and V. Sandoghdar, *Nature Reviews Methods Primers*, 2025, **5**, 23.
40 S. Berciaud, D. Lasne, G. A. Blab, L. Cognet and B. Lounis, *Physical Review B—Condensed Matter and Materials Physics*, 2006, **73**, 045424.
41 S. Berciaud, L. Cognet, G. A. Blab and B. Lounis, *Phys. Rev. Lett.*, 2004, **93**, 257402.

View Article Online
DOI: 10.1039/D5NH00801H

Data availability statement

Data supporting this article have been included as part of the Supplementary Information.